Journal of Power Sources 195 (2010) 4905–4914

Contents lists available at ScienceDirect

Journal of Power Sources

journal homepage: www.elsevier.com/locate/jpowsour

Thermal stresses in an operating micro-tubular solid oxide fuel cell

Mustafa Fazil Serincan [a,*], Ugur Pasaogullari [a], Nigel M. Sammes [b]

[a] Department of Mechanical Engineering, and Center for Clean Energy Engineering, University of Connecticut, 44 Weaver Rd., Unit 5233, Storrs, CT, 06269, USA
[b] Department of Metallurgical and Materials Engineering, Colorado School of Mines, 1500 Illinois St, Golden, CO, 80401, USA

ARTICLE INFO

Article history:
Received 9 November 2009
Received in revised form
18 December 2009
Accepted 22 December 2009
Available online 14 January 2010

Keywords:
SOFC
Micro-tubular
Thermal stress
Ceria-based electrolyte
Composite

ABSTRACT

A multi-physics model is developed to investigate the thermal stresses in a micro-tubular SOFC, based on a previously developed thermal-fluids model predicting cell operation. Mechanical properties of the anode and cathode are determined theoretically through composite structure approximation. Residual stresses arisen during the fabrication of the cell due to the mismatch in thermal expansion coefficients are calculated by accounting for each fabrication process separately. The interactions between the cell, the sealant and the alumina tube are accounted for a better representation of the actual fuel cell test setup. The effect of sealant and alumina tube on the stress distribution in the cell is investigated and it is found out that near the fuel cell–sealant interface stress distribution changes significantly. The effect of spatial temperature gradient on the stress distribution is also analyzed and found to have a minimal impact for a typical fuel cell operation at mid-range current densities. The effects of oxygen vacancies caused by the reduction of the GDC electrolyte on the overall stress distribution are also shown. Oxygen vacancies of the electrolyte result in relaxation of the stresses due to the alleviation of mismatch in Young's modulus between different layers of the cell.

1. Introduction

Amidst the discussions on global warming and the concerns about limited fossil fuel resources, solid oxide fuel cells (SOFCs) have been accepted as one of the most promising candidates for an alternative power generation method because of their low pollutant emissions and fuel flexibilities [1,2]. As well as being used as standalone energy conversion devices with high power densities, due to their elevated operating temperatures SOFCs can also be considered in combined heat and power applications for increased system efficiencies [3,4].

Albeit their advantages, SOFCs are yet to become commercial, primarily due to high fabrication costs and reliability issues. Regarding the fabrication costs, planar type SOFCs are more favorable than tubular type because of their compact designs and simpler manufacturing processes [5]. Regarding the durability and reliability of the fuel cells, difficulty in obtaining mechanical stability and necessity for more sophisticated sealing arrangements make tubular design superior to planar design. Indeed miniaturizing the tubular cells to sub-millimeter dimensions, i.e. micro-tubular SOFC, is reported to result in better thermal cycling and shock resistance capabilities and hence, improved mechanical durability [6].

Thermal stresses are the main factors for the failure of not only the fuel cell but also the sealants. Thermal stresses can be induced in the materials by several ways; however those related to fabrication of the cell (residual stresses) are the most critical. During the cooling of the cell after being sintered at very high temperatures, stresses arise in the materials due to the mismatch in thermal expansion coefficients (TEC) between different layers of the cell. However, residual stresses can also be expected if the cooling rates are not slow enough to sustain a quasi-steady heat transfer resulting in spatial temperature gradients. Furthermore, spatial temperature gradients during the fuel cell operation, mechanical loading of the cell, and the mismatch in the properties of the chosen sealant and support tube materials also determine the thermal stresses induced in the cell.

In the context of thermal stresses, it should be mentioned that a specific case arises for the SOFCs, which employ ceria-based electrolytes, such as gadolinia-doped ceria (GDC), yttria doped ceria (YDC), or samaria doped ceria (SDC). In fuel cell operating conditions, Ce^{4+} is reduced to Ce^{3+}, which results in oxygen vacancies in the electrolyte [7–9]. This results in electron transport from the anode to cathode, also known as leakage currents, which decreases the cell voltage at low current densities. Reduction of the electrolyte also affects the crystal structure of the material and hence the mechanical properties such as Young's modulus and TEC [10,11]. Therefore, in an SOFC with a ceria-based electrolyte, thermal stresses also depend on the reduction of the electrolyte.

* Corresponding author. Tel.: +1 8609493526; fax: +1 8604868378.
E-mail address: fazil.serincan@engr.uconn.edu (M.F. Serincan).

0378-7753/$ – see front matter © 2010 Published by Elsevier B.V.
doi:10.1016/j.jpowsour.2009.12.108

Nomenclature

A	pre-exponential constant
C_p	specific heat
D	elasticity matrix
D_{jk}	binary diffusivities
E	Young's modulus
F	Faraday constant
$F_{r/z}$	force components
$\mathbf{g}$	gravity
G	shear modulus
i	transfer current density
$\mathbf{I}$	identity matrix
h	enthalpy
k	thermal conductivity
K	bulk modulus
K_p	permeability
m	reactant dependency
MW	molecular weight
$\mathbf{N}$	mass flux
p	pressure
Q	volumetric heat source
r	radial coordinate
R	universal gas constant
R_j	volumetric consumption of the jth species
T	temperature
$\mathbf{u}$	velocity vector
V	volume fraction
w	species mass fraction
x	species mole fraction
z	axial coordinate

Greek symbols

α	thermal expansion coefficient
$\alpha_{a/c}$	transfer coefficient
ε	normal strain
ϕ	potential
γ	shear strain
η	overpotential
φ	porosity
κ	conductivity
μ	dynamic viscosity
ν	Poisson's ratio
ρ	density
σ	normal stress
τ	shear stress
θ	tangential

Subscripts

0	initial
a	anode
c	cathode
comp	composite
e	electronic
eff	effective
el	elastic
i	ionic
j	species
k	species
r	radial
ref	reference
th	thermal
z	axial

Superscripts

eff	effective
eq	equilibrium
low	lower bound
T	transpose
Th	thermal
up	upper bound

Cell components subject to extensive thermal stresses fail by brittle fracture, and the failure modes differ whether the failure is in tensile or in compression. Tensile failure generally occurs as a result of crack propagation whereas compressive failure, an unusual failure mode for ceramics, generally occurs as a result of interfacial delamination [12]. Due to the imperfections during the SOFC fabrication, it is highly possible that cracks may exist in the cell, which could initiate failure under tensile stresses. Therefore, thermal stresses in tensile state are not desirable and the cells should be designed and operated to minimize tensile stresses.

Since thermal stresses are the main reasons for the mechanical failure of the SOFCs, prediction of stresses by finite element analysis (FEA) is important to understand the failure modes, suggest design and operation guidelines and to assess mechanical durability of the cells. Two types of analyses are possible: predicting the residual stresses in the standalone SOFC at room temperature and predicting the stresses in an operating SOFC held in a test fixture. The former takes into account only the stresses in the cell components due to mismatch in TECs, whereas the significance of the latter arises from the inclusion of the exterior loading in the analysis and the interactions between the cell, sealant and the supporting tubes.

Only a few work in the open literature so far focus on the mechanical analysis of SOFCs, which are mostly on planar SOFCs. Some of these works concentrate on calculations of solely the residual stresses at room temperature [13–15]. For an operating SOFC, Yakabe et al. [16] and Selimovic et al. [17] calculated stresses for planar design, whereas Nakajo et al. [18] and Cui and Cheng [19] have studied tubular design. However, all of these studies neglect the interactions between the cell and the peripheral components such as seals or gaskets and therefore do not represent the actual stress field in a fuel cell operation. Models taking into account these interactions in an operating SOFC can be found in the studies of Lin et al. [20] and Nakajo et al. [21], which focus on planar SOFC stacks, and the work of Weil and Koeppel [22], which emphasize on the sealant design. However, these studies lack the detailed representation of the cell due to computational concerns, and the cell is modeled as a single component without considering anode, electrolyte and the cathode separately. The most rigorous study on thermal stress analysis is the one by Nakajo et al. [21], in which an anode supported planar SOFC stack is analyzed. In the FEA, the interactions between the cell, electrodes, gaskets and interconnects are taken into account. The temperature field is calculated via a CFD model, but the cathode is not included in stress calculations and the cell consists of anode and electrolyte only.

In this study, we present a detailed mechanical analysis of a micro-tubular SOFC subject to thermal stresses arising from fabrication of the cell, exterior constraints, and fuel cell operation. We calculate the thermal stresses based on the temperature field obtained from previously developed thermal-fluids model [22]. We also predict the residual stresses considering each sintering process separately carried out in the course of cell fabrication. Furthermore, based on the experimental setup of a micro-tubular SOFC reported [24], we include the sealant and the supporting tubes in our stress calculations not only to account for the exterior stress loading on

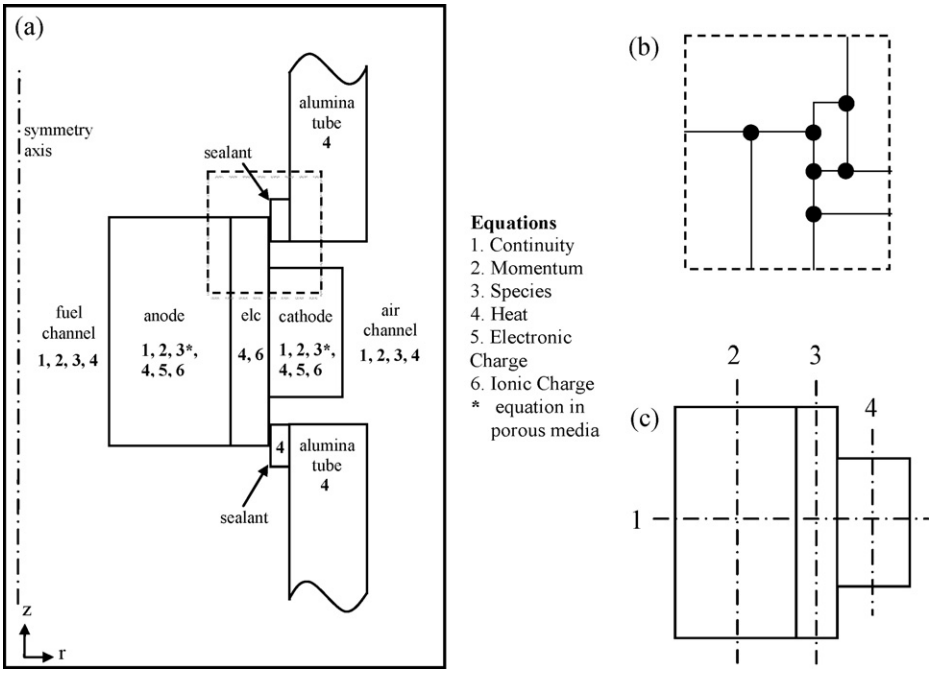

Fig. 1. (a) Model geometry. (b) Singularities in the upper half geometry. Black dots show the singularity points where mesh refinements are required. Plotted region is represented with dashed lines in (a). (c) The lines where profiles are drawn along. Profiles are discussed in Section 4.

the cell components but also to predict the thermal stresses in the sealant.

Anode and cathode electrodes used in the cells consist of two different materials each and can be represented as a composite structure. Although, mechanical properties can be widely found in the literature for pure anode and cathode materials, the values for the composite electrode structure should deviate significantly from the pure material properties. Hence, in this study we use the theory of composite materials to determine the mechanical properties for composite electrode structures. Non-stoichiometry effects on the mechanical properties of the ceria-based electrolyte are also considered. Determination of the material properties is explained in the modeling section.

2. Mathematical model

We utilize the thermal-fluid model we previously developed [23–25] and use the predicted temperature distribution in the mechanical analysis. The geometry of the previous model is extended to include the sealants that are applied between the electrolyte coating and the supporting alumina tubes as seen in Fig. 1. The model geometry presented is based on the experimental setup of Suzuki et al. [26]. We use their cell performance data to validate our model predictions, therefore predicted cell temperatures are expected to closely represent the experiments.

Model geometry includes the anode tube and the fuel channel, the electrolyte, the cathode and the air chamber, sealants and the supporting alumina tubes. Due to the axial symmetry of the tubular geometry, the model is constructed in a 2-dimensional axisymmetric domain by assuming the current collectors are uniformly distributed on the electrode surfaces.

2.1. Thermal-fluids model

Thermal-fluids model has been explained comprehensively in Refs. [23,24], and governing equations are summarized here in Table 1 for completeness. The model predicts the transport of mass, momentum, species, energy and charge, as well as electrochemical kinetics of anode and cathode reactions. Source terms appearing in the governing equations are listed in Table 2. Mass, species and momentum conservation equations are solved in the gas channels and the porous electrodes, and energy conservation is applied to the entire domain. Ionic charge balance is applied in the anode, the electrolyte and the cathode whereas the electronic charge balance is applied in the anode and the cathode.

It should be noted that momentum equation (Eq. (2)) is written in general form and valid for both gas phase and porous regions where the porosity, φ and the permeability, K_p is unity and infinity for the open channels, respectively. Also, in porous regions we modify species equation (Eq. (3)) in order to implement dusty gas model

Table 1
Governing equations of the thermal-fluid model.

Mass	$\nabla \cdot (\rho \mathbf{u}) = R_j$	(1)
Momentum	$\rho \mathbf{u} \cdot \nabla \mathbf{u} = \nabla \cdot \left[-p\mathbf{I} + \mu/\varphi \left(\nabla \mathbf{u} + (\nabla \mathbf{u})^{\mathrm{T}} \right) - 2\mu/3 (\nabla \cdot \mathbf{u}) \mathbf{I} \right] + \rho \mathbf{g} - \left(\mu/K_p \right) \mathbf{u}$	(2)
Species	$\nabla \cdot \left[\rho w_j \mathbf{u} - \rho w_j \sum_{k=1}^{n} \tilde{D}_{jk} \left(\nabla x_k + (x_k - w_k) \nabla p/p \right) \right] = R_j$	(3)
Energy	$\nabla \cdot (-k \nabla T + \rho C_p T u + \sum_j h_j \mathbf{N_j}) = Q$	(4)
Electronic charge	$-\nabla \cdot (\kappa_e \nabla \phi_e) = i_{a/c}$	(5)
Ionic charge	$-\nabla \cdot (\kappa_i \nabla \phi_i) = -i_{a/c}$	(6)

Table 2
Source terms of the thermal-fluid model.

Mass and species	$R_j = \pm(i_{a/c}/nF)MW_j$	(7)
Momentum	$F = u\sum_j R_j$	(8)
Energy	$Q = (E_{max} - V_{cell})\, i_a$	(9)
Anode transfer current	$i_a = A_a \exp\left(-EA_a/RT\right)\left(x_{H_2} p/x_{H_2}^{ref} p_{ref}\right)^{m_{H_2}}\left(x_{H_2O} p/x_{H_2O}^{ref} p_{ref}\right)^{m_{H_2O}} \sin h\left(\frac{\alpha_a F}{RT}\eta_a\right)$	(10)
Cathode transfer current	$i_c = A_c \exp\left(-EA_c/RT\right)\left(x_{O_2} p/x_{O_2}^{ref} p_{ref}\right)^{m_{O_2}} \sin\ h\left(\frac{\alpha_c F}{2RT}\eta_c\right)$	(11)

which accounts for Knudsen diffusion in small pores. Furthermore, in the porous regions assuming thermal equilibrium between the gas phase and the solid phase heat equation is formulated by volume averaging as described in [27]. For further details the reader is referred to Refs. [23,24].

2.2. Solid mechanics model

2.2.1. Constitutive relations

It is assumed that ceramic cell materials, sealant and the alumina tube undergo linear (elastic) deformation when subject to thermal loads. Total strain consists of elastic, thermal and initial contributions such that

$$\varepsilon = \varepsilon_{el} + \varepsilon_{th} + \varepsilon_0 \tag{12}$$

where the strain components for an axi-symmetric system are [28]

$$\varepsilon_r = \frac{\partial u}{\partial r}, \quad \varepsilon_\theta = \frac{u}{r}, \quad \varepsilon_z = \frac{\partial w}{\partial z}, \quad \gamma_{rz} = \frac{\partial u}{\partial z} + \frac{\partial w}{\partial r} \tag{13}$$

which are normal strains in radial, tangential, axial (longitudinal) direction and shear strain in the *rz* plane respectively.

Thermal strain is calculated as

$$\varepsilon_{th} = \alpha\,(T - T_{ref}) \tag{14}$$

where α is the thermal expansion coefficient (TEC) of the material. T, temperature field is taken from the solution of the thermal-fluids model, and T_{ref} is the stress free temperature at which there is no stress accumulated in the material. Determining the stress free temperature is very critical as it directly affects the magnitude of the thermal stress induced in the material. For SOFCs it is widely accepted that T_{ref} is the sintering temperature at which different layers are joined [13–21].

Stress–strain relationship for a linear elastic material is given as:

$$\sigma = D\varepsilon_{el} + \sigma_0 \tag{15}$$

which can be rewritten using Eq. (12) as

$$\sigma = D\,(\varepsilon - \varepsilon_{th} - \varepsilon_0) + \sigma_0 \tag{16}$$

where σ_0 is the initial stress distribution which represents the residual stresses in our model. D, the elasticity matrix, for an isotropic material in axial symmetry is defined for axial symmetry as following:

$$D = \frac{E}{(1+\nu)(1-2\nu)}\begin{bmatrix} 1-\nu & \nu & \nu & 0 \\ \nu & 1-\nu & \nu & 0 \\ \nu & \nu & 1-\nu & 0 \\ 0 & 0 & 0 & \frac{1-2\nu}{2} \end{bmatrix} \tag{17}$$

where E defines the Young's modulus and ν is the Poisson's ratio of the material.

2.2.2. Equilibrium equations

The equilibrium equations for axial symmetry are [28]:

$$\frac{\partial \sigma_r}{\partial r} + \frac{\partial \tau_{rz}}{\partial z} + \frac{\sigma_r - \sigma_\theta}{r} = F_r \tag{18}$$

$$\frac{\partial \tau_{rz}}{\partial r} + \frac{\partial \sigma_z}{\partial z} + \frac{\tau_{rz}}{r} = F_z \tag{19}$$

in radial and axial directions, respectively. Here, σ_r, σ_θ, σ_z, represent the normal stresses in radial, tangential and axial direction respectively while, τ_{rz} represents the shear stress in *rz* plane.

2.2.3. Determination of the material properties

In the anode supported micro-tubular cells we consider here, gadolinia-doped ceria $Ce_{0.9}Gd_{0.1}O_{1.95-\delta}$ (GDC) electrolyte is coated on porous NiO-GDC anode, and $La_{0.8}Sr_{0.2}Co_{0.6}Fe_{0.4}O_3$ (LSCF)-GDC is used as cathode. Mechanical properties for the dense anode and cathode are calculated using the relations given for heterogeneous materials based on "composite sphere method" (CSM) [29,30]. This method takes the composite material as a spherical matrix of one phase and the spherical impurities of the other phase that are concentrically placed in the matrix. Hashin and Shtrikman [30] calculated the bounds for the bulk and shear moduli of composite material theoretically as

$$K_{comp}^{low} = K_1 + \frac{V_2}{1/(K_2 - K_1) + 3V_1/(3K_1 + 4G_1)} \tag{20}$$

$$K_{comp}^{up} = K_2 + \frac{V_1}{1/(K_1 - K_2) + 3V_2/(3K_2 + 4G_2)} \tag{21}$$

$$G_{comp}^{low} = G_1 + \frac{V_2}{1/(G_2 - G_1) + 6V_1(K_1 + 2G_1)/[5G_1(3K_1 + 4G_1)]} \tag{22}$$

$$G_{comp}^{up} = G_2 + \frac{V_1}{1/(G_1 - G_2) + 6V_2(K_2 + 2G_2)/[5G_2(3K_2 + 4G_2)]} \tag{23}$$

where K and G corresponds to the bulk and shear modulus of the material and V is the volume fraction of each phase in the composite material. Expressions for the lower bound are derived when first phase is assumed to be the matrix and the second phase being the impurities. The upper bounds are calculated when the reverse is assumed.

It is suggested that properties of any arbitrary composite material stays in between these bounds [30]. Budiansky suggested an exact implicit solution for the bulk and shear moduli and Poisson ratio [31]. For the anode and cathode, the upper and lower bounds calculated from Hashin's expressions are observed to be identical hence they are used in our model instead of Budiansky's relations.

Expressions for the effective elastic and shear moduli for the porous media are given by the approach developed by Ramakrishnan and Arunachalam [32,33]. This approach is based on CSM considering the pores instead of the impurities. There are also empirical expressions to determine the porous material properties [34–36]. Selcuk and Atkinson [37] compared these models with

Table 3
Material properties.

	E (GPa)	ν	TEC ($\mu m\,m^{-1}$)	ρ ($kg\,m^{-3}$)
Ni	219 [43]	0.313 [43]		8900 [43]
GDC	See text	0.334 [44]		7150 [44]
LSCF	161 [45]	0.320 [45]		6820 [45]
Anode			11.8 [42]	
Electrolyte			11 [42]	
Cathode			13 [42]	
Sealant	90[a]	0.31[a]	7.74 [46]	3990 [46]
Alumina tube	400 [43]	0.22 [43]	8 [46]	3965 [43]

[a] Assumed.

their experimental data. Due to the good agreement with the experimental data and its simplicity, CSM is used here due to simplicity. Effective Young's modulus and shear modulus are determined as,

$$E_{\text{eff}} = E_0 \frac{(1-\varphi)^2}{1+(2-3\upsilon_0)\varphi} \tag{24}$$

$$G_{\text{eff}} = G_0 \frac{(1-\varphi)^2}{1+(11-19\upsilon_0)/(4-4\upsilon_0)\varphi} \tag{25}$$

where φ is the porosity of the medium. Subscript 0 stands for the properties of the dense materials.

As discussed earlier, reduction of Ce^{4+} to Ce^{3+} results in oxygen non-stoichiometry in GDC, which affects the thermoelastic properties of the material. To account for this, elastic modulus of GDC is characterized as a function of oxygen partial pressures as given in Ref. [10]. A curve fit to the experimental data is:

$$E_{\text{GDC}} = a + b\left(-\log_{10} p_{O_2}\right)^c \tag{26}$$

where $a = 255.9 \times 10^9$ Pa, $b = 3.31 \times 10^{-5}$ and $c = 11.11$ ($R^2 = 0.995$).

Oxygen partial pressure for different operating conditions is given by Steele [38] for a typical GDC electrolyte. The distribution of the oxygen partial pressure in the electrolyte can be calculated as explained in Refs. [8,39]. For different operating voltages the distribution will be different as the oxygen partial pressure is related to the reduction of the electrolyte. However, we incorporate an approximate distribution based on Riess [8] for simplicity.

The effect of oxygen vacancies on the thermal expansion coefficient of GDC is also reported in [40]. However, for operating temperatures lower than 600 °C, the effect is insignificant compared to that at higher temperatures. In addition to the thermal expansion, the defect concentration in the material also results in chemical expansion, as defined by Adler [41]. Chemical expansion of the GDC as a function of oxygen partial pressure is given in [11], however, it is not included here since it is not significant at temperatures below 600 °C.

While Young's moduli and Poisson's ratios are determined using above relations based on the mechanical properties for pure materials, TECs of the anode, the electrolyte and the cathode are obtained from Ref. [42], where they are experimentally determined for a temperature range of 25–650 °C. The values are listed in Table 3 along with the Young's moduli and Poisson's ratios for Ni, GDC and LSCF. Table 3 also lists the mechanical properties for sealant and alumina tube.

2.2.4. Boundary conditions

In the experiments, the cell is fixed to alumina tubes from each side by the sealant. The assembly is then placed inside another tube and the outer tube is fixed to the furnace horizontally. This way, inner tubes move freely without being imposed any constraints except the linear contact with the outer tube. Assuming the gravitational forces have negligible contribution to the overall stress distribution, the boundary conditions are set to free deformation. However, to set a reference point bottom of the alumina tube is fixed in axial direction.

3. Numerical implementation

Model equations are solved in a commercial multi-physics software, COMSOL, which uses finite element method to discretize the partial differential equations (PDEs). COMSOL has the capability of coupling the thermo-fluid model with the solid mechanics model in the single file, which makes it convenient for solving problems including thermal-structure interactions. Since this coupling is assumed to be one way i.e., temperature field affects the stress distribution but not the other way, model equations are solved sequentially: first the thermal-fluids model is solved and then predicted temperature field is used in solid mechanics model.

Sequential solution procedure also allows us to develop a rational meshing strategy as following: thermal-fluid model solves for 11 variables (pressure, velocity components, species, temperature and potentials) at every node of each mesh element, therefore requires a higher computational effort, compared to the solid mechanics model which solves for only 2 (radial and axial displacements) variables. Also due to high non-linearity fashion of the model equations and the strong coupling between them, long computational times are required to solve for the thermal-fluids model. Hence, number of mesh elements needs to be adjusted carefully to minimize the computational time without compromising the accuracy of the solution. With the COMSOL's flexibility of choosing different types of elements in the same geometry, the thermal-fluids model consists of 3799 triangular and 1940 quadrilateral mesh elements. Although this mesh topology is tested to be good enough for the thermal-fluids model, it is not satisfactory for the solid mechanics model. The main problem arising with the solid mechanics calculations are the singularities existing at the corners of two different layers or two different materials where the magnitude of the stress tends to infinity. Hence the mesh needs to be refined at these singularities. Fig. 1b shows the singularities in the upper half model geometry. In the geometry considered in the solid mechanics model, there are 12 singularities and mesh refinements at these points are carried out for solid mechanics calculations. 43,590 triangular elements are used in the solid mechanics model for a reasonable performance at the singularities. This is 12 times of that used in thermal-fluid model.

Non-linear set of equations is solved with Newton iteration and then one of the linear solvers in COMSOL's library are utilized for the rest of the solution [47]. On a workstation equipped with a quad-core X5355 INTEL XEON processor and 8 Gb of RAM, the solution for the thermal-fluid model takes around 10 min whereas solid mechanics model takes only 15 s. Although the latter employs more elements, the big difference in the solution time can be attributed to the highly non-linear model equations, the number of variables to be solved and the strong coupling in the thermal-fluid model.

4. Results

With the model described in previous section simulations are performed to predict the stress distribution in the fuel cell and the sealant. The effects of different factors on the stress distribution are also investigated.

4.1. Residual stresses

To calculate the residual stresses developed during cell fabrication, each fabrication process needs to be known. The micro-tubular SOFCs we consider here are taken from AIST, Japan and we refer to Suzuki et al. [24] who described the fabrication processes of

these cells. These processes are summarized briefly as: anode tube is extruded and left to dry. Then it is dip coated with electrolyte slurry. Electrolyte coated cells are then sintered at 1450 °C. After cooled down to room temperature (RT) as slow as 5 °C min^{-1}, cathode coating is applied to the tubes. The whole cell is then sintered at 1050 °C and then the PEN (positive-electrolyte-negative) structure is cooled down to room temperature again in a controlled way. Fabricated cells then go through a redox cycling before being tested. Finally they are attached to the alumina tubes with Ceramabond sealing material at room temperature and they become ready for the electrochemical tests.

It is possible residual stresses exist in each step. Since it is very difficult to estimate the residual stresses induced in the anode during the extrusion of the tubes, we do not consider them in this study. Also, we assume that electrolyte coating and cathode pasting do not induce residual stresses. Therefore, we only account for sintering processes as the sources for residual stresses. Since the structures are cooled to room temperature very slowly, i.e. 5 °C min^{-1}, in a temperature-controlled furnace, we assume that the process is quasi-static such that the spatial temperature gradients existing in the structure are negligible. Therefore we assume that the residual stresses are induced in the anode/electrolyte and PEN structures only due to the TEC mismatch between different layers.

We first calculate the residual stresses induced during sintering of the anode/electrolyte structure, taking the stress free temperature as 1450 °C. Due to higher TEC of the anode, 11.8 μm m^{-1}, than that of the electrolyte, 11 μm m^{-1}, anode tends to shrink more when the structure is cooled down to room temperature. However, since this action is restrained by the electrolyte, tensile stresses exist in the anode support which is compensated by the compressive stresses induced in the electrolyte coating. The profiles of the axial component of normal stress along the horizontal centerline of the anode/electrolyte structure (line 1 in Fig. 1c) are shown in Fig. 2a. Due to the large aspect ratio of the tubes, i.e., length/width = 25/1, no radial distribution is observed in the profiles. Since the electrolyte coating is much thinner than the anode wall thickness, the magnitudes of the residual stresses are different in the anode and the electrolyte. Shear stress is negligible compared to axial normal stress, so the integral of axial normal stress taken over the anode volume would be equal to that taken over the electrolyte volume with an opposite sign (recall Eq. (17)). This is implied by the force equilibrium of the entire structure when there is no external force acting on the system.

The stresses arisen during the second sintering process, which includes the cathode coating on the tube, are calculated based on the residual stresses induced during the previous sintering process. Residual stresses calculated at 1050 °C for the first process are given as initial stress fields for the anode and electrolyte whereas at this temperature cathode is assumed to be stress free. Residual stresses in the PEN structure are seen in Fig. 2b. Since both anode and cathode have higher TEC than that of the electrolyte, tensile stresses are observed in these layers whereas compressive stresses are seen in the electrolyte. Comparing Fig. 2a and b, it is also observed that, the magnitude of the compressive stress increased at the electrolyte at the room temperature because in the PEN structure electrolyte restrains the shrinkage of not only the anode but the cathode as well due to the force equilibrium, as discussed in previous paragraph.

Room temperature is the most critical condition that an unsupported SOFC experiences [12]. If the support conditions are chosen carefully, an operating SOFC is not exposed to stresses as high as residual stresses at the room temperature. As seen in Fig. 2b at a typical operating condition of an intermediate temperature SOFC, relaxation of the residual stresses are experienced as the stress free temperature is approached.

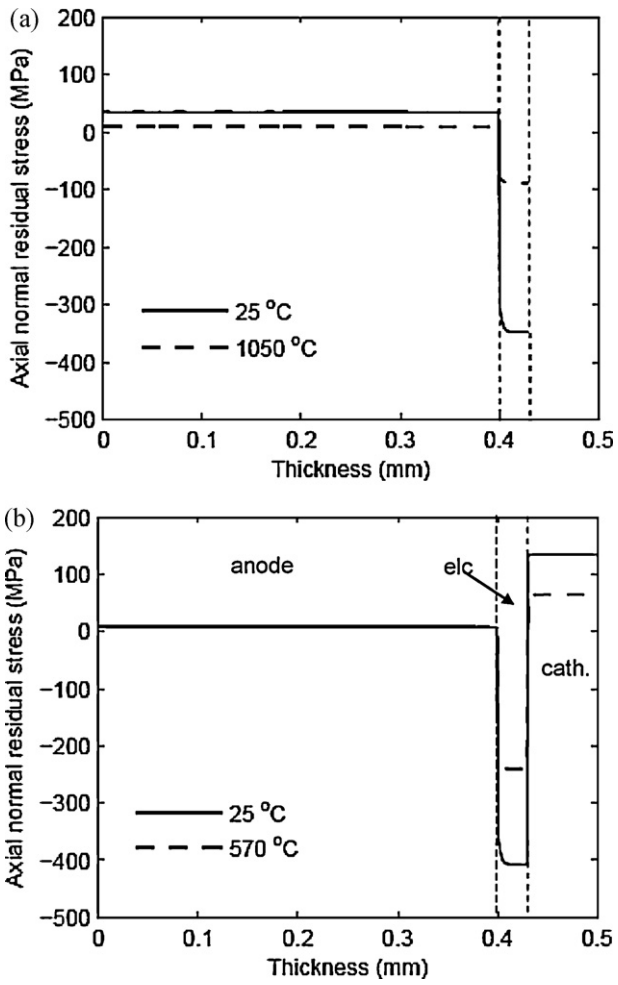

Fig. 2. Residual stresses arisen after (a) the first sintering process in the anode and the electrolyte (b) second sintering process in the whole cell. The profiles are drawn along the horizontal centerline (line 1 of Fig. 1c).

4.2. Thermal stress during SOFC operation

Stress distribution in an operating micro-tubular SOFC is predicted with the calculated residual stresses given as initial stress fields. SOFC is attached to the alumina tubes with the sealant applied between the electrolyte coating and the inner surface of the tubes at room temperature. Therefore the stress free temperature for the assembly is taken as 25 °C as no stress is assumed to build up at the interfaces of the sealant between the cell and the tubes. However, residual stresses exist in the cell components.

With the predicted temperature distribution of a micro-tubular SOFC operating potentiostatically at 0.7 V, thermal stresses occurring during the operation are calculated. In the actual SOFC operation, fuel is supplied to the cell as a mixture of 20 vol% hydrogen and 80 vol% nitrogen at a flow rate of 25 cm^3 min^{-1} whereas ambient air is used at the cathode. The furnace temperature is controlled at the air channel as 550 °C while overpotentials cause a higher temperature in the cell. As seen in Fig. 3 it is predicted that the maximum temperature in the cell to be 561 °C at 0.7 V (∼11 °C higher from furnace temperature). However, as reported previously [23], the cell temperature may increase by as much as 120 °C at 0.2 V.

The test assembly consisting of the cell, sealants and the alumina tubes undergoes an elastic deformation when heated up to the cell operating conditions from room temperature. The scaled deformation of the assembly is seen in Fig. 4 where gray lines show the

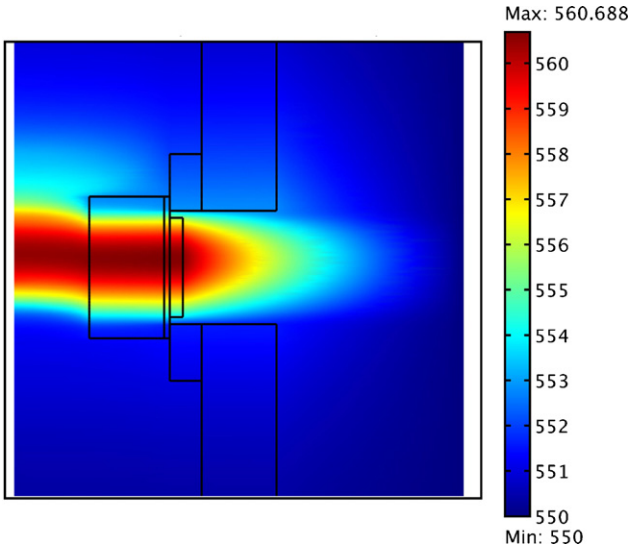

Fig. 3. Predicted temperature distribution in C for the SOFC operating at 0.7 V.

undeformed structure. Contours on the deformed shape show the axial elongation. Although the structure deforms freely, i.e. without any constraints, it is fixed axially at the bottom of the alumina tube as a reference. Since cell components have higher TECs than sealant and the alumina tube, cell tends to expand more both in radial and axial direction. However, movement of the cell is restricted by the sealant. Therefore a non-homogeneous deformation is observed in the cell, such that the middle regions of the cell expands radially more than those supported by the sealant. On the other hand, as implied by the Newton's third law of motion, the PEN structure forces the corresponding regions in the sealant and the alumina tube to expand radially.

Corresponding axial normal stress distribution in the cell, sealant and the alumina tube are shown in Fig. 5 which portrays only a portion of the model geometry. Figure is drawn to scale.

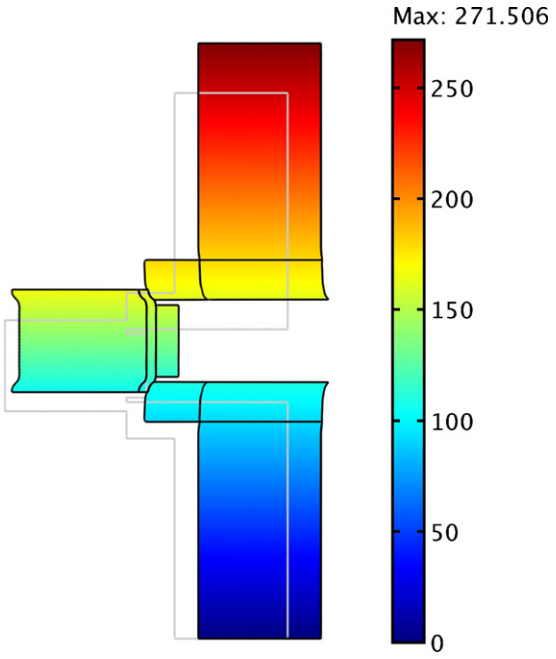

Fig. 4. Deformation of the assembly under thermal stresses. Gray lines show the undeformed shape. Contours show the axial elongation distribution in microns on the deformed shape.

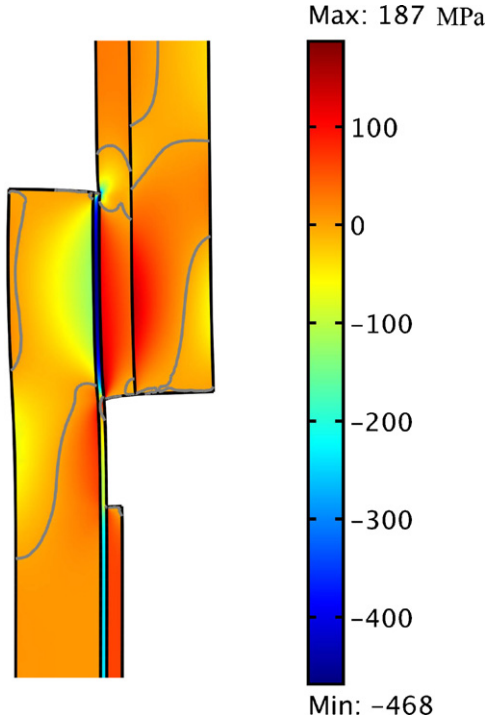

Fig. 5. Axial stress distribution in the cell, sealant and the alumina tube is plotted on the deformed shape (deformation is scaled 40 times for clarity). Contours show the transition of the stress from compression to tension, i.e. $\sigma_z = 0$. (the figure is drawn to scale.)

Negative values of stress show compression, where positive values show tension. Tensile and compressive stresses may coexist in a single layer. This is due to the combined effects of residual stresses and the interactions between different components of the assembly. However, a very big portion of anode, sealant and alumina tube are in tension whereas electrolyte is in compression. Observation of the cell components experiencing two different stress states at the same time is reported first for a tubular SOFC in this study.

The profiles in Fig. 6 show the components of the normal stress along the centerline of the electrolyte (line 3 in Fig. 1c). The first observation is that the magnitudes of the axial and tangential stress components converge to the same value at the region exposed as a plateau in the profiles. This behavior is shown to be true for thin walled cylindrical structure with a high aspect ratio [48]. It is also seen that the magnitude of the radial normal stress is much less than those of the other two components.

4.3. Effect of the support structure on the stress distribution

Axial normal stress profiles at 0.7 V are shown in Fig. 7a. The profiles are drawn along the vertical centerlines (lines 2–4 in Fig. 1c) of each layer. Fig. 7b shows the residual stress contribution for each case. Since residual stresses are calculated for an unsupported cell, the differences between the profiles in Fig. 7a and b are due to the interaction between the cell and the support components in the test assembly. When the profiles for the cathode in both figures are compared, there is a little difference observed, which suggests that almost all the contribution to the axial stress distribution is due to residual stresses, since cathode has no interaction with the peripheral components. When the profiles in Fig. 7a and b are compared for the electrolyte, it is observed that the magnitudes of the stresses corresponding to the plateaus in these profiles are almost same. However, the magnitude of the axial stress profile deviates from that of the residual stress profile at the regions close to the electrolyte–sealant interface. This is also true for the change in the

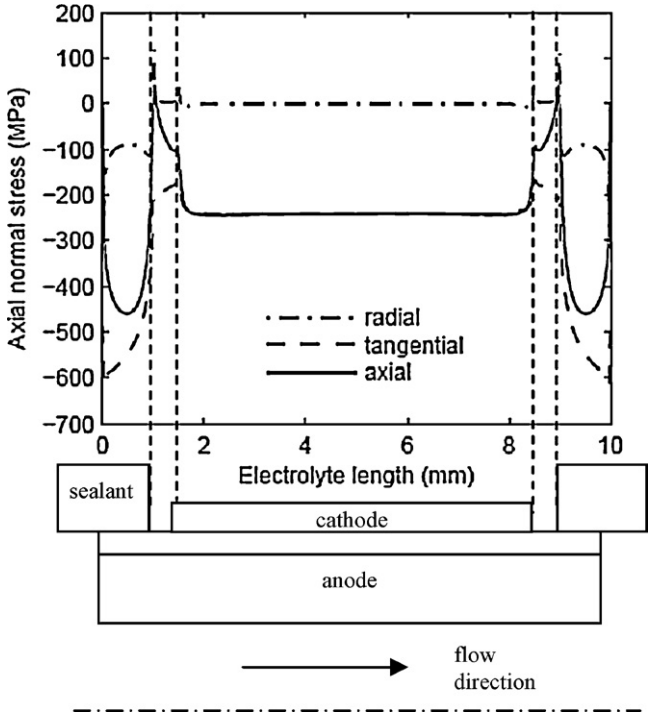

Fig. 6. Normal stress components along the vertical centerline of the electrolyte. The illustration below the figure depicts the cell assembly. The profile is drawn along the vertical centerline of the electrolyte (line 3 of Fig. 1c).

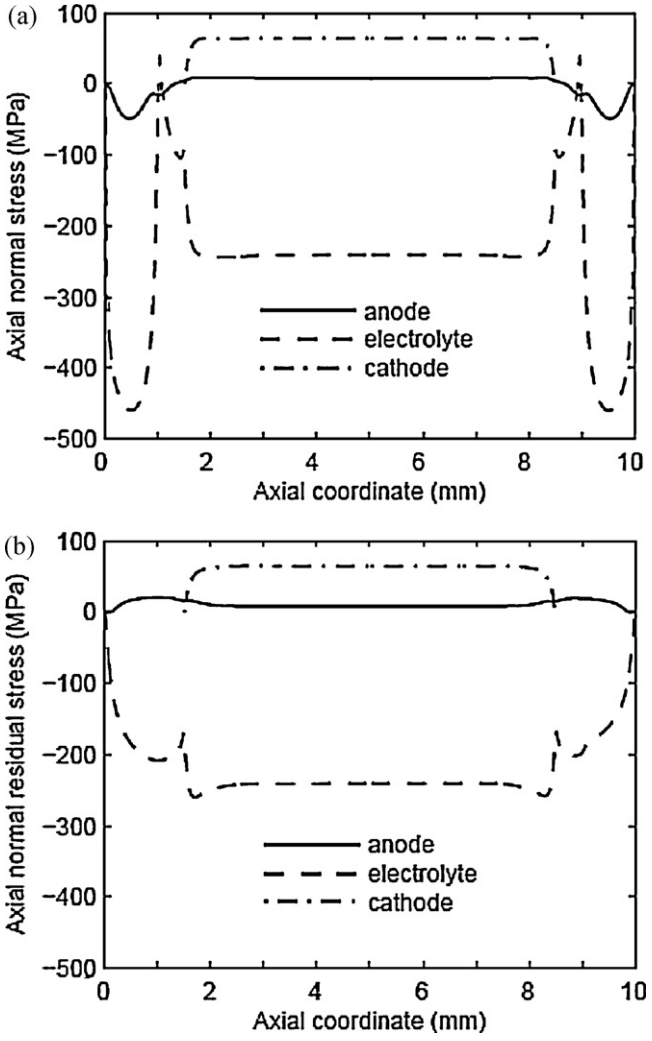

Fig. 7. (a) Axial stress profiles in the anode, electrolyte and cathode along the vertical centerlines of each layer (lines 2–4 in Fig. 1c). (b) Corresponding residual stress contributions (due to sintering) for each layer.

sign of the axial stress profiles. As it is seen in Fig. 7b, residual stress is in pure tension in the anode whereas axial normal stress becomes compressive at the regions close to the electrolyte–sealant interface. Note that at each end of the tube, axial stress value is equal to zero because these points correspond to the free surfaces.

Axial stress profile is shown in Fig. 8 along the vertical centerline of the electrolyte (line 3 in Fig. 1c). There are three different trends seen in the profile: corresponding to the regions of the electrolyte supported by the sealant (0–1 mm and 9–10 mm), the regions of the electrolyte that are coated with the cathode (1.5–8.5 mm) and the free regions of the electrolyte between the cathode coating and the support tube (1–1.5 mm and 8.5–9 mm). As discussed before, the trend in the profile exposed as a plateau, is mainly due to the residual stresses. Departing from the plateau, the portion of the profile corresponding to the free regions of the electrolyte has an increasing trend which suggests that in these regions there is a tensile stress contribution to the overall profile. Free regions of the electrolyte do not have any radial constraints, and tend to expand radially more than the other regions. This can be seen in Fig. 5 as parts of the electrolyte corresponding to the free surface are warped outwards. However, radial expansion of these regions is restricted with the constraints posed by both the sealant from the above and the cathode coating from the below. An analogy to a beam clamped from both sides can be used to explain this. If the beam is under a distributed transverse loading, tensile stresses are induced in its cross-section. Similarly, tensile stresses in axial direction are induced in the electrolyte. Nevertheless, the overall axial stress in the electrolyte is still in compression due to the contribution of the residual stresses except the regions closer to the sealant interface.

The portion of the profile corresponding to the electrolyte regions supported with the sealant has first a decreasing then an increasing trend. The first trend suggests an extra compressive contribution to the overall axial stress. This is due to the large TEC mismatch between the electrolyte and the sealant. Electrolyte material GDC has a TEC of 11 while it is 7.8 for the Ceramabond 552 sealant. As a result when heated up to operating temperature, compressive stresses are introduced in these regions in addition to the inherent residual stresses which are also in compression. As a result compressive stresses as high as 570 MPa are predicted in the electrolyte. The axial stresses however, vanish at the free surface of the electrolyte; therefore after reaching the maximum the stress profile has a decreasing trend.

4.4. Effect of temperature gradient

Other than TEC mismatch, spatial temperature variations in the materials may induce thermal stresses as well. To distinguish between this and TEC mismatch, stresses are calculated based on a uniform temperature field, which is the controlled temperature in the furnace. Then they are compared with the overall stress field calculated based on the temperature distribution in a cell operating at 0.2 V. The difference between these two is attributed to the effect of temperature gradients on the thermal stresses. Shown in Fig. 9a are the axial stress profiles along the electrolyte centerline. The temperature profile along the same line is also seen in Fig. 9b. The regions of the electrolyte that experience higher temperature tend to expand more. However, this will be restricted by the regions of the cell that have lower temperature. Therefore

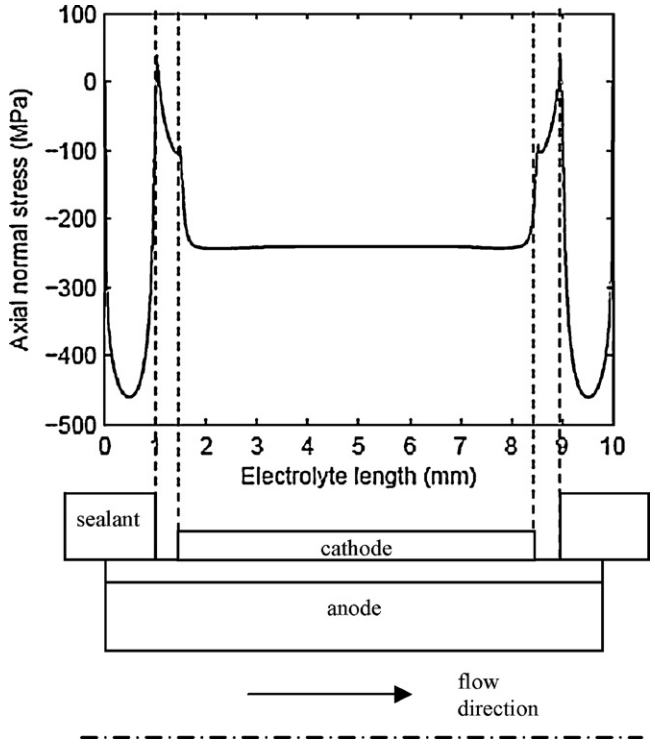

Fig. 8. Axial normal stress profile along the electrolyte centerline. The profile is drawn along the vertical centerline of the electrolyte (line 3 of Fig. 1c).

hotter electrolyte regions will experience tensile stresses whereas colder regions will be under compression. Since the temperature profile is not symmetric but shifted towards the flow outlet due to the effect of convection, maximum tensile is also observed towards the flow outlet. Hence, to balance the tensile stresses greater compressive stresses are induced at the upper regions of the electrolyte than those induced at the lower regions.

4.5. Effect of oxygen defects on the elasticity of the electrolyte

The reduction of Ce^{4+} to Ce^{3+} in CeO_2 causes oxygen vacancies in the GDC lattice structure. This increases the average bond length which causes the elasticity of the material to decrease [11]. Oxygen vacancies also change the expansion behavior of the material. However, it is reported that this effect is only significant at temperatures above 600 °C, below that linear thermal expansion is observed [10]. Since we consider an IT-SOFC operating at 550 °C, the effect of oxygen vacancies on TEC are neglected providing that the temperature increase is calculated to be less than 50 °C for a typical fuel cell operating voltage of 0.7 V. The effect of oxygen vacancies on the elasticity of the electrolyte is accounted for, however. In Fig. 10, axial stress profiles along the horizontal centerline of the electrolyte (line 1 in Fig. 1c) are seen for GDC with defects (reduced) and that without defects. Young's modulus of GDC is higher than both Ni and LSCF. With the reduction of GDC elasticity due to the oxygen vacancies, the difference between anode and cathode moduli of elasticity decreases. Hence the stress distribution induced in the electrolyte is alleviated. The axial stress drops by as much as 20% at the anode-electrolyte interface with the introduction of the defects in GDC.

Young modulus of GDC is calculated via Eq. 22 based on the oxygen partial pressure distribution in the electrolyte. The model does not solve for oxygen partial pressure implicitly, rather an assumed profile is used in Eq. 22. Riess solved for oxygen partial pressure distribution in the electrolyte for different operating conditions [8].

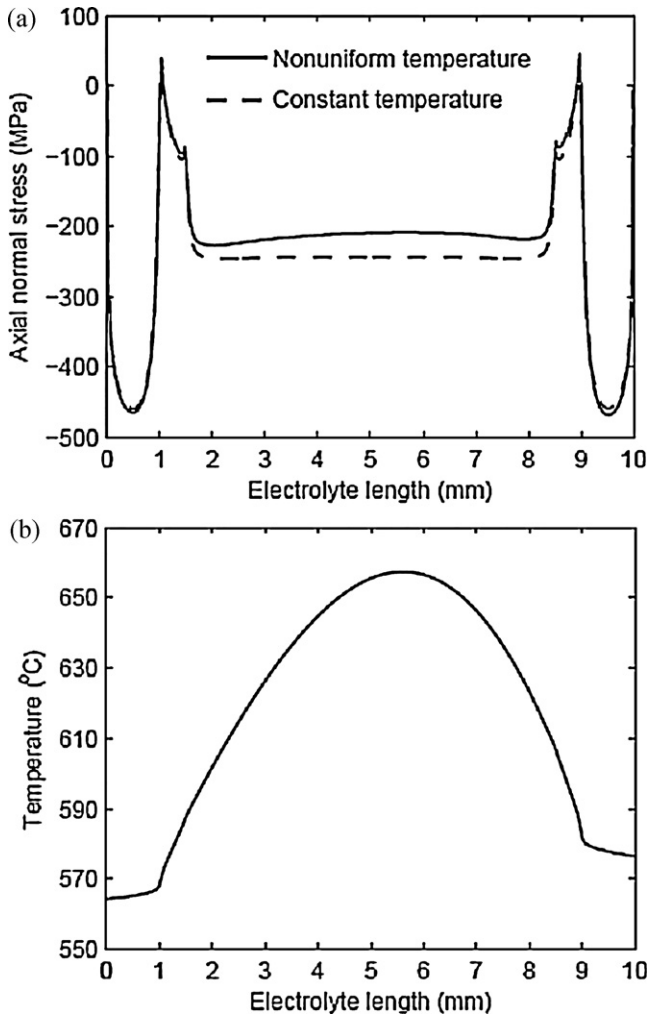

Fig. 9. (a) Effect of temperature gradient on the axial normal stress profile. Solid line is the predicted profile for the cell under actual operating conditions; dashed line is for the hypothetical case when the uniform cell temperature is 550 °C. (b) Temperature profile for the cell operating at 0.2 V. The profiles are drawn along the vertical centerline of the electrolyte (line 3 of Fig. 1c).

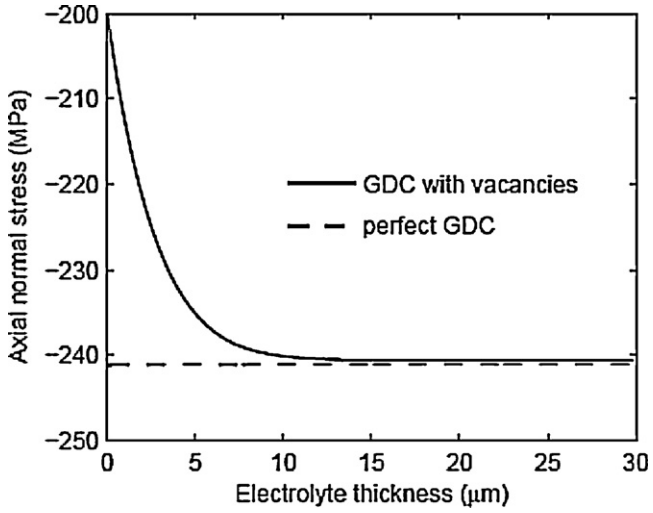

Fig. 10. Effect of oxygen vacancies in GDC on the axial stress distribution. Solid line predicts the stress profile for the actual electrolyte, dashed line is for the hypothetical case when the electrolyte has no defects. Profiles are drawn along the horizontal centerline (line 1 of Fig. 1c).

Consistent with his results at 0.7 V, we assume a logarithmic profile in the radial direction based on which we calculate the Young's modulus.

5. Conclusions

A solid mechanics model is developed to investigate the thermal stresses in a micro-tubular SOFC. Mechanical properties of the cell are determined by approximating anode and cathode as composite structures. The fabrication processes are modeled to calculate the residual stresses. Applying the residual stresses as initial stress fields, thermal stresses are calculated based on the temperature field calculated by the thermal-fluid model.

We address and distinguish the effects of different factors determining the stress distribution in the cell components: i) residual stresses, ii) exterior stress loading due to the interactions with the peripherals, iii) temperature gradients presented during the fuel cell operation, iv) effects of oxygen vacancies in the ceria-based electrolyte. Residual stresses are determinant on the overall stress field in the bulk of the cell layers while the interactions between the cell and the support structure have significant effects on the stress distribution. Due to these interactions, we observe that both compressive and tensile stresses can exist in the same layer simultaneously. We have also found out that the effect of the spatial temperature distribution is minimal for a typical SOFC operation at mid-range current densities. We also see that because of the alleviation of the mismatch in Young's moduli between electrolyte and the neighboring layers, stresses in the electrolyte decreases with the introduction of the oxygen vacancies in GDC.

The thermal-fluid model used in this work is only validated against the performance data obtained by Suzuki et. al. [26], and this validation is shown in Ref. [23]. We have verified the computational solution of the solid mechanics model by method of manufactured solutions (MMS) [49], which tests the computational model against a known analytical solution. We have also performed grid independence studies. However, verification only ensures the correctness of the numerical solution; it validates neither the material properties nor the correctness of the developed physical model. Therefore, an experimental validation needs to be performed in order to ensure the accuracy of the results and validity of our conclusions.

In a stress analysis of an operating SOFC it is paramount to include the sealant and the alumina tube in the solid mechanics model. For the results shown here, for moderate operating current densities, a uniform temperature field can be used to calculate thermal stresses. However, at higher current densities temperature gradients must be calculated.

Acknowledgement

This work was supported by New Energy Development Organization (NEDO) of Japan and the School of Engineering at the University of Connecticut.

References

[1] N.Q. Minh, T. Takahashi, Science and Technology of Ceramic Fuel Cells, Elsevier, Amsterdam, 1995.
[2] S.C. Singhal, K. Kendall, High Temperature Solid Oxide Fuel Cells: Fundamentals, Design and Applications, Elsevier, Kidlington/Oxford/Amsterdam, 2003.
[3] A. Hawkes, P. Aguiar, C.A. Hernandez-Aramburo, M. Leach, N.P. Brandon, T.C. Green, C.S. Adjiman, J. Power Sources 156 (2006) 321.
[4] K. Alanne, A. Saari, I.V. Ugursal, J. Good, J. Power Sources 158 (2006) 403.
[5] N.M. Sammes, Y. Du, R. Bove, J. Power Sources 145 (2005) 428.
[6] W. Bujalski, C.M. Dikwal, K. Kendall, J. Power Sources 171 (2007) 96.
[7] B.C.H. Steele, Solid State Ionics 134 (2000) 3.
[8] I. Riess, J. Electrochem. Soc. 128 (1981) 2077.
[9] M. Godickemeier, K. Sasaki, L.J. Gauckler, I. Riess, Solid State Ionics 86–88 (1996) 691.
[10] Y. Wang, K. Duncan, E.D. Wachsman, F. Ebrahimi, Solid State Ionics 178 (2007) 53–58.
[11] K. Duncan, Y. Wang, S. Bishop, F. Ebrahimi, E. Wachsman, J. Am. Ceram. Soc. 89 (2006) 3162.
[12] A. Atkinson, B. Sun, Mater. Sci. Technol. 23 (2007) 1135.
[13] H. Yakabe, Y. Baba, T. Sakurai, Y. Yoshitaka, J. Power Sources 135 (2004) 9.
[14] T. Zhang, Q. Zhua, W.L. Huang, Z. Xie, X. Xin, J. Power Sources 182 (2008) 540.
[15] J. Laurencin, G. Delette, F. Lefebvre-Joud, M. Dupeux, J. Eur. Ceram. Soc. 28 (2008) 1857.
[16] H. Yakabe, T. Ogiwara, M. Hishinuma, I. Yasuda, J. Power Sources 102 (2001) 144.
[17] A. Selimovic, M. Kemm, T. Torisson, M. Assadi, J. Power Sources 145 (2005) 463.
[18] A. Nakajo, C. Stiller, G. Harkegard, O. Bolland, J. Power Sources 158 (2006) 287.
[19] D. Cui, M. Cheng, J. Power Sources 192 (2009) 400.
[20] C.K. Lin, T.T. Chen, Y.P. Chyou, L.K. Chiang, J. Power Sources 164 (2007) 238.
[21] A. Nakajo, Z. Wuillemin, J. Van Herle, D. Favrat, J. Power Sources 193 (2009) 216.
[22] K.S. Weil, B.J. Koeppel, Int. J. Hydrogen Energy 33 (2008) 3976.
[23] M.F. Serincan, U. Pasaogullari, N.M. Sammes, J. Electrochem. Soc. 155 (2008) B1117.
[24] M.F. Serincan, U. Pasaogullari, N.M. Sammes, J. Power Sources 192 (2009) 414.
[25] M.F. Serincan, U. Pasaogullari, N.M. Sammes, J. Power Sources 194 (2009) 864.
[26] T. Suzuki, T. Yamaguchi, Y. Fujishiro, M. Awano, J. Electrochem. Soc. 153 (2006) A925.
[27] A. Faghri, Y. Zhang, Transport Phenomena in Multiphase Systems, Academic Press/Elsevier Inc., Burlington, MA, 2006, p. 993.
[28] R.T. Fenner, Mechanics of Solids, CRC Press, 1989.
[29] Z. Hashin, J. Appl. Mech. 29 (1962) 143.
[30] Z. Hashin, S. Shtrikman, J. Mech. Phys. Solids 11 (1963) 127.
[31] B. Budiansky, J. Mech. Phys. Solids 13 (1965) 223.
[32] N. Ramakrishnan, V.S. Arunachalam, J. Mater. Sci. 25 (1990) 3930.
[33] N. Ramakrishnan, V.S. Arunachalam, J. Am. Ceram. Soc. 76 (1993) 2745.
[34] R.E. Fryexell, B.A. Chandler, J. Am. Ceram. Soc. 47 (1964) 283.
[35] R.M. Spriggs, J. Am. Ceram. Soc. 44 (1961) 628.
[36] D.P.H. Hasselman, J. Am. Ceram. Soc. 54 (1962) 452.
[37] A. Selcuk, A. Atkinson, J. Eur. Ceram. Soc. 17 (1997) 1523.
[38] B.C.H. Steele, Solid State Ionics 129 (2000) 95.
[39] M. Godickemeier, L.J. Gauckler, J. Electrochem. Soc. 145 (1998) 414.
[40] S. Wang, M. Katsuki, T. Hashimoto, M. Dokiya, J. Electrochem. Soc. 150 (2003) A952.
[41] S.B. Adler, J. Am. Ceram. Soc. 84 (2001) 2117.
[42] S. Hashimoto, H. Nishino, Y. Liu, K. Asano, M. Mori, Y. Funahashi, Y. Fujishiro, J. Electrochem. Soc. 155 (2008) B587.
[43] COMSOL 3.4 Material Library, Burlington, MA (2007).
[44] K. Sato, H. Yugami, T. Hashida, J. Mater. Sci. 39 (2004) 5765.
[45] Y.S. Chou, J.W. Stevenson, T.R. Armstrong, L.R. Pederson, J. Am. Ceram. Soc. 83 (2000) 1457.
[46] www.matweb.com, 2009.
[47] COMSOL, COMSOL 3.4, Multiphysics Reference Guide, COMSOL, Burlington, MA, 2007.
[48] A. Kandil, A.A. El-Kady, A. El-Kafrawy, Int. J. Mech. Sci. 37 (1995) 721.
[49] P.J. Roache, J. Fluids Eng. 124 (2002) 4.